Enhancing Exposure Efficiency and Uniformity Using a Choke Ring Antenna: Application to Bioelectromagnetic Studies at 60 GHz

Artem V. Boriskin, *Senior Member, IEEE*, Maxim Zhadobov, *Member, IEEE*, Sergiy Steshenko, *Member, IEEE*, Yves Le Dréan, Laurent Le Coq, Christian Person, *Senior Member, IEEE*, and Ronan Sauleau, *Senior Member, IEEE*

Abstract—An effective solution for increasing the exposure uniformity and efficiency of biological samples in *in vitro* bioelectromagnetic experiments at 60 GHz is proposed by introducing a novel choke ring antenna (CRA). The CRA is optimized to provide a uniform exposure of samples, whose dimensions are equivalent to those of a standard 35-mm Petri dish, positioned close to the antenna aperture, i.e., 10–20 wavelengths. The antenna prototype is fabricated in metallized foam. The realized exposure efficiency of the sample exceeds 55% (if estimated for an exposure uniformity better than -0.5 dB). To validate the numerical results, the field intensity profiles on the surface of a high-water-content phantom have been experimentally obtained using a high-resolution infrared camera. Compared to the standard open-ended waveguide and horn antennas, typically used for millimeter-wave dosimetry, a twofold advantage of the proposed CRA is demonstrated, namely, the improvement of the exposure efficiency by a factor of 1.5 to 2 with a simultaneous reduction of the exposure distance by a factor of 8–2, respectively, depending on the type of the reference antenna. These advantages make the proposed CRA an excellent candidate for 60-GHz short-range exposure systems for *in vitro* bioelectromagnetic studies.

Index Terms—Bioelectromagnetics, choke ring antenna (CRA), dosimetry, exposure efficiency, exposure system, metallized foam, millimeter waves, 60 GHz, uniform illumination, waveguide feed.

I. INTRODUCTION

F UTURE commercialization of *V*-band devices and mass production of 60-GHz high-data-rate communication systems have raised concerns about possible health risks associated
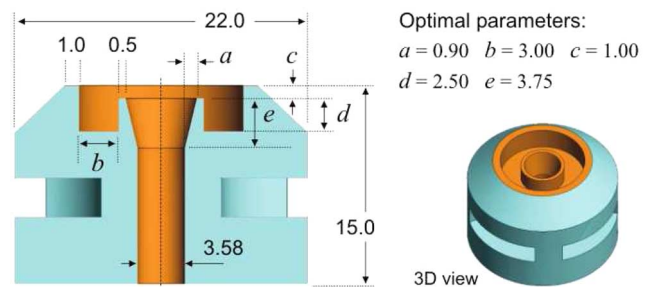

Fig. 1. Cross-sectional and 3-D views of the proposed CRA. All dimensions are in millimeters. Control parameters adjusted through optimization are denoted by Latin letters. The antenna body is fabricated in dielectric foam (shown in blue in online version). Metallized surfaces are highlighted in orange (in online version).

with interactions between millimeter waves, absent in the natural electromagnetic background, and the human body [1].

Bioelectromagnetic studies are conducted to characterize potential biological impacts of such radiations and their power thresholds. This implies a well-controlled exposure of biological samples. For this purpose, a number of exposure systems have been developed based on standard waveguide feeds [1]–[10]. The performance characteristics of such feeds are reviewed in the Appendix. Their common weak points with respect to the target exposure specifications are: 1) insufficient uniformity for the power density distribution at the surface of the sample under test (SUT) and 2) low exposure efficiency. Thus, development of new antenna systems enabling better control over these exposure characteristics is necessary.

This paper aims at the development of an exposure system enabling the optimal illumination conditions for *in vitro* bioelectromagnetic experiments in the 60-GHz band. In this framework, a novel choke ring antenna (CRA) is designed and optimized (Fig. 1). Selection of the CRA among other possible antenna solutions (existing alternatives at microwaves and millimeter waves are discussed in [11] and [12] and [1]–[10], respectively) is due to the following advantages offered by the CRA:

- compact size (low perturbation due to the backscattering from high-contrast biological samples);
- large opening angle (short-range exposure);
- shaped-beam pattern (uniform illumination);
- ease of integration with a waveguide feeding system (low insertion loss/high exposure levels).

A.V. Boriskin, M. Zhadobov, L. Le Coq, and R. Sauleau are with the Institut d'Electronique et de Télécommunications de Rennes (IETR), UMR CNRS 6164, Université de Rennes 1, Rennes 35042, France (e-mail: artem.boriskin@ieee.org; maxim.zhadobov@univ-rennes1.fr).

S. Steshenko is with the Institute of Radiophysics and Electronics of the National Academy of Sciences of Ukraine (IRE NASU), Kharkov 61085, Ukraine.

Y. Le Dréan is with the Institut de la Recherche sur la Santé, l'Environnement et le Travail (IRSET), INSERM U1085, Université de Rennes 1, Rennes 35042, France.

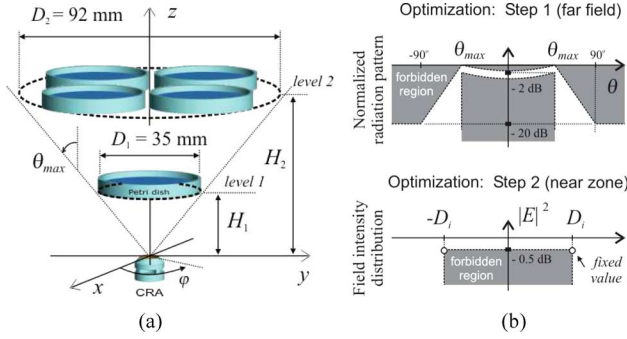C. Person is with the Lab-STICC, UMR CNRS 6285, Brest 29238, France.

Fig. 2. (a) Exposure scenarios. (b) Optimization templates (not to scale).

These advantages made CRAs a favorable solution for various applications, including diathermy applicators for the near-field heating [13], primary feeds for large reflector antennas [14]–[18], communication with satellites [19]–[21], and low-multipath GPS antennas [22]. In this work, for the first time, the CRA is used as a radiating structure for a millimeter-wave dosimetric system. A preliminary research and physical analysis of waveguide antennas with corrugated flanges have been reported in [23] and [24].

To enable fast and low-cost experimental verification of the proposed concepts, the CRA is prototyped in metallized foam, according to procedure reported in [25] and [26]. To the best of our knowledge, this is one of the very first antennas in metallized foam with operational frequency as high as 60 GHz.

II. ANTENNA CONFIGURATION AND DESIGN METHODOLOGY

A. Target Application

Compact feeds, enabling a constant flux short-range exposure, are of interest for many applications [13]–[24]. Such a feed can also find certain applications in bioelectromagnetics.

The proposed antenna is intended to become a constitutive part of a 60-GHz exposure system developed recently for exposure of human cells; it will replace the currently used standard pyramidal horn antenna [6], [9]. A detailed description of the system is provided in [6], and is thus omitted here.

The details relevant to the current studies are the following. In the experiments, the biological samples are placed at the bottom of a standard tissue culture plate (consisting of six 35-mm wells) and positioned as shown in Fig. 2(a). Typical exposure scenarios include illumination of one or four wells of the culture plate located at the level 1 or 2, respectively. To improve the exposure efficiency, the antenna configuration is optimized as discussed below.

B. Antenna Configuration

A computer-aided design (CAD) model of the proposed CRA is shown in Fig. 1. The antenna consists of a section of a standard circular waveguide ending with a conical horn surrounded by a choke ring whose rim is slightly extended above the horn aperture. Compared to earlier studies [15], two additional control parameters are used (namely, horn flare depth and diameter)

to provide additional degrees of freedom for optimizing the antenna performance characteristics with respect to the specific exposure uniformity requirements. The antenna is fabricated in metallized foam, which results in reduction of the fabrication costs and improvement of the antenna performance, namely, a better symmetry of the main beam and lower sidelobe level (SLL) achieved due to natural suppression of the edge currents, which can be induced on the metal surfaces.

The antenna profile is controlled by five variables denoted by Latin letters (Fig. 1), whose optimal values are determined through optimization. The other parameters are defined based on the following considerations.

- *Rim thickness* of the horn and choke ring is chosen in a way to preserve a sufficient rigidity of the structure, but not affect the symmetry of the antenna radiation pattern. As discussed in [23] and [24], there is a strong difference in the impact of the metallic flange on the antenna patterns in the E-plane (TM polarization) and H-plane (TE polarization), which is a corollary of the electromagnetic behavior of the E- and H-waves in the vicinity of a metallic boundary.
- *Diameter of the antenna and its backside configuration* are defined to fit with a standard V-band circular waveguide flange (UG-385/U).
- *External wall thickness* is increased to approximately 5 mm to reinforce the structure; its rim is cut at 45° in a way to obtain a desired width of the metallized rim of the outer ring.
- *Length of the waveguide section* (9.55 mm) is selected to be slightly larger than the guided wavelength ($\lambda_g \approx 8.7$ mm at 60 GHz); this helps diminish the impacts of the higher modes, which can be excited at the discontinuity between the metallic waveguide and CRA fabricated in metallized foam.

The antenna is fed by a standard circular waveguide ($\emptyset = 3.58$ mm) operating in the fundamental TE_{11} mode.

C. Optimization Procedure

As already discussed, there are two major requirements formulated for the exposure system, namely: 1) uniform illumination of the SUT and 2) high exposure efficiency. The latter parameter can be defined as a ratio of the useful power (incident on the SUT surface) with respect to the total radiated power. This efficiency definition is used instead of the one based on the specific absorption rate (SAR) or total absorbed power because we aim to characterize the antenna performance regardless to the SUT type. An additional figure of merit of the system is the exposure distance, i.e., the distance between the antenna and SUT at which the desired illumination condition is satisfied. Large exposure distance raises certain difficulties including precise positioning of the sample, increase of the setup dimensions, and lower incident power density, which is critical at millimeter waves. Thus, reduction of the exposure distance becomes an important issue.

To design an antenna satisfying the aforementioned requirements, a two-step optimization procedure is followed.

First, the CRA control parameters are optimized to get a symmetrical radiation pattern with a secant square beam and the

widest possible opening angle (the latter is needed to reduce the exposure distance). At this step, the cost function is defined as misfit between the actual and desired radiation patterns

$$F_c^1 = \sum_{(f)} \sum_{(\varphi)} \sum_{(\theta)} \left| G_f(\varphi, \theta) - G_0^1(\varphi, \theta) \right| \text{(dB)} \qquad (1)$$

where G_f is the antenna gain at a certain frequency f and G_0^1 is a function defining the secant square beam template [see Fig. 2(b)]. The opening angle of the secant beam $\theta_{\max}$ is selected empirically, i.e., maximized in order to reduce as much as possible the exposure distance $H_1 = D_1/(2\tan\theta_{\max})$. The pattern symmetry is controlled in four vertical cut planes ($\varphi = 0°, 30°, 60°, 90°$). In addition, the reflection coefficient criterion is set as $S_{11} < -20$ dB. Although the antenna is intended to operate in the narrow band of 60 GHz $\pm 1\%$, the cost function is calculated at three frequency points, namely, $f = 58, 60,$ and 62 GHz. The multi-frequency optimization is used to compensate for a possible deviation of the antenna geometrical parameters due to fabrication tolerances.

After that, the antenna configuration is tuned with respect to the template, which defines uniformity of the energy flux through the sample surface [see Fig. 2(b)]

$$F_c^2 = \sum_{(x)} \sum_{(y)} \{P_{f_0}(x, y, H_1) - G_0^2\}$$
$$+ E \, [\text{dB}(\text{W/m}^2)] \qquad (2)$$
$$P_{f_0}(x, y, H_1) = 20 \cdot \log(E(x, y, H_1)/E_{\max})$$
$$E = \sum_{(x)} \sum_{(y)} \left\{ \left| P_{f_0}(x, y, H_1)\right|_{x,y \in L} \right| - 0.5 \right\}$$

where $f_0 = 60$ GHz, G_0^2 is a function defining the penalty for escaping the -0.5-dB corridor, $E_{\max}$ is the peak value of the E-field magnitude in the plane (x, y, H_1), and L is a contour of SUT 1 (i.e., circle with diameter D_1). The second term in (2) is used to fix the edge illumination level at the desired -0.5 dB.

Note that both cost functions are defined with respect to the illumination conditions of SUT 1 (i.e., a single well with diameter $D_1 = 35$ mm), whereas the optimal exposure distance and exposure efficiency for SUT 2 (i.e., four wells with an equivalent diameter $D_2 = 92$ mm) is determined later for the already defined antenna configuration. Both exposure scenarios are shown schematically in Fig. 2(a).

Finally, the exposure efficiency is determined for both samples and arbitrary exposure uniformity levels either by estimating the energy flux through the sample surface or by calculating the energy radiated in the given angular sector $d\Omega$ (i.e., $-\theta_{\max} \leq \theta \leq \theta_{\max}$ and $0 \leq \varphi \leq 2\pi$). The obtained quantities are then normalized by the total radiated power. The latter definition is computationally simpler because it accounts only for the antenna gain; however, it does not guarantee the desired uniformity and edge illumination conditions, which is critical for short exposure distances). Thus, the former definition is more appropriate and is used hereafter. It is derived as follows:

$$\eta_e = \frac{1}{P_{\text{rad}}} \int\!\!\int_A S \, dA \qquad (3)$$
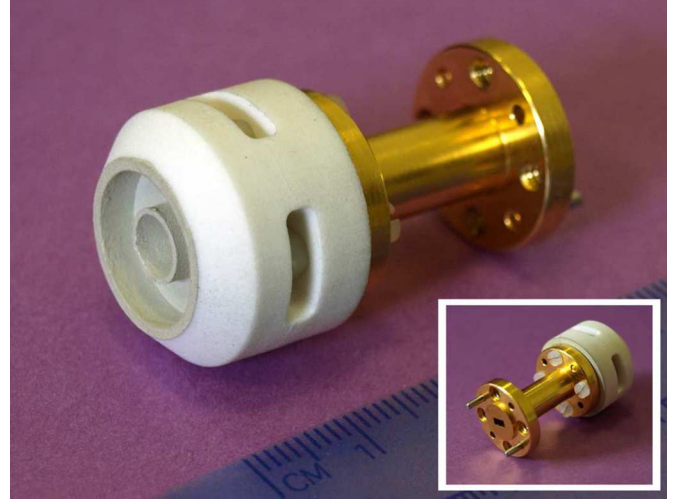

Fig. 3. Antenna prototype attached to a standard V-band circular-to-rectangular waveguide transition. Metallized surfaces of the foam antenna front-end are seen in a light grey color.

where S is the time-averaged magnitude of the Poynting vector, $A = \pi D_1^2/4$, and P_{rad} is the total radiated power.

All simulations are carried out using full-wave commercial software FEKO [27]. The optimization technique used at both steps is the steepest descent gradient methods implemented in FEKO with initial values derived according to [15], [23], and [24]. The exposure efficiency is then determined by post-processing of the near- and far-field data. For the reported CRA and selected exposure distances, the difference between the two definitions discussed above does not exceed 1%.

III. NUMERICAL AND EXPERIMENTAL RESULTS

A. Antenna Prototype

The antenna prototype (Fig. 3) has been fabricated using the process described in [25]. This process consists of micro-machining the 3-D-shaped body of the antenna in a foam bulk material with a computer numerically controlled lathe and its further metallization using silver spray painting (Spraylat Cu/Ag conductive coating). As reconfirmed by direct measurements using a microscope (Nikon MM-40), the deviation of the prototype dimensions from the specification varies in between 10–50 μm. This difference is associated both with the fabrication tolerance and finite thickness of the metallization layer. Our estimate for the latter is about 10–30 μm for the external (easy to reach) and internal (difficult to reach) surfaces, respectively. Note that metallization thickness cannot be controlled easily, although it defines the layer conductivity, and thus affects the prototype performance.

The material used for the antenna fabrication is a commercially available dielectric foam Eccostock LoK ($\varepsilon_r = 1.8, \tan\delta = 0.0028$ in Ka-band [26]). The favorable features of the selected material are: 1) light weight; 2) sufficient rigidity; and 3) slightly rough surface, which is good for the metallization purpose. In addition, the selected foam has low water absorption, which allows one to use it inside incubators with high humidity.
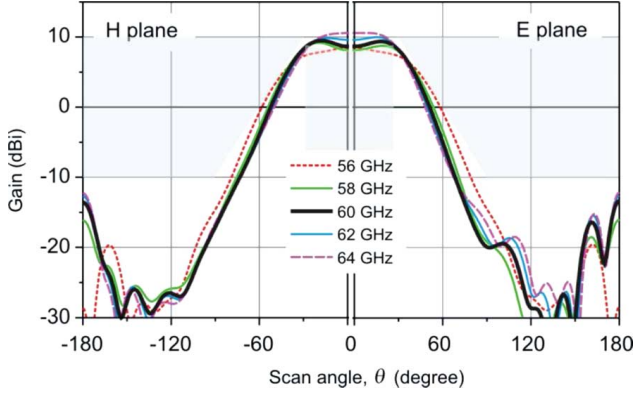
Fig. 4. Simulated radiation pattern of the reported CRA in H-plane (left axis) and E-plane (right axis). The family of five curves describes patterns computed at different frequencies (see legend).
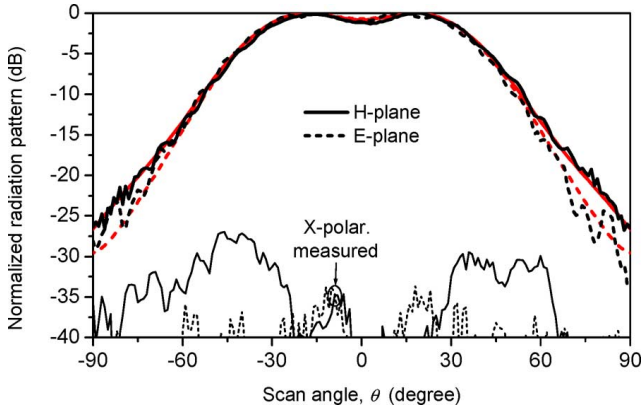

Fig. 5. Measured (black) and simulated (red in online version) normalized radiation patterns at 60 GHz: (solid line) H-plane; (dashed line) E-plane.

Fig. 6. CRA reflection coefficient.

Fig. 7. CRA boresight gain.

B. Radiation Characteristics

The simulated radiation patterns of the optimized CRA computed at five frequency points in both principal planes are plotted in Fig. 4. The patterns have a specific mono-lobe shape, perfectly-symmetric with nearly flat top and very low SLL. Its shape well satisfies the optimization template with $\theta_{\max} = 30°$ (shown via the grey color) and remains stable within the desired frequency range of 58–62 GHz. The parametric study shows that minor deviations of the control parameters (i.e., ± 0.2 mm from the optimal values) do not change the pattern (these data are skipped for brevity).

The CRA radiation characteristics are measured in the millimeter-wave anechoic chamber of IETR, which is routinely used for the antenna characterization from 18 to 110 GHz. The co- and cross-polarization patterns measured at 60 GHz are shown in Fig. 5. An excellent agreement between the measured and simulated data is observed within the entire angular range. The measured cross-polarization level is below -27 dB, assuring a pure linear polarization that is important for some biological tests (e.g., neuron development under millimeter-wave exposure). On the other hand, the rotational symmetry of the antenna structure and its radiation pattern, together with the low cross-polar level, enables one to use this CRA for illuminating circular samples in a circular polarization regime.
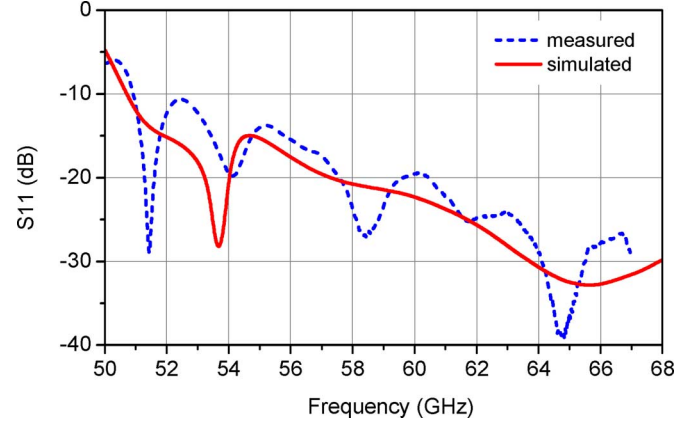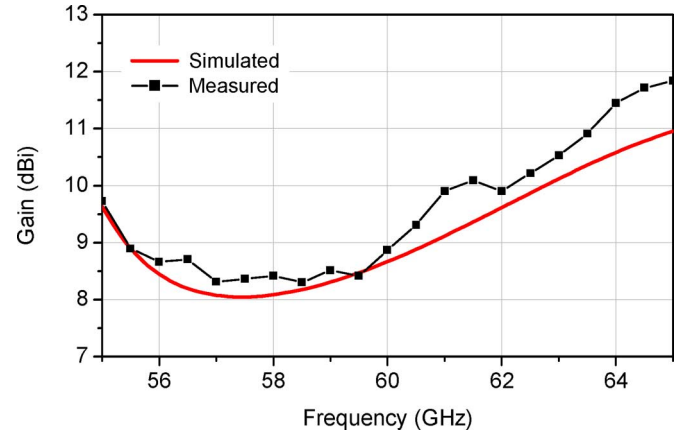
The simulated and measured reflection coefficients S_{11} of the reported CRA are shown in Fig. 6. In the range of interest (58–62 GHz), S_{11} remains below -19 dB. The resonance observed in simulations near to 54 GHz is due to the choke ring. The other three periodic resonances observed for the measured reflection coefficient can be due to the rectangular-to-circular waveguide transition (not included in calibration) or due to the waveguide discontinuity at the junction between the waveguide and CRA.

The boresight gain of the antenna is shown in Fig. 7. In simulations, metallization thickness is assumed to be constant (10 μm), and conductivity value is equal to 3.3×10^7 S/m (according to the manufacturer specifications for a dry film with the selected thickness). The dielectric loss is also taken in consideration.

C. Exposure Characteristics

As we aim at the highest possible exposure efficiency (under the desired -0.5-dB exposure uniformity), the field distribution in the plane coinciding with the SUT surface is analyzed here in addition to the far-field performance characteristics presented in Section II-B.

Fig. 8 represents the E-field magnitude along the antenna physical axis (left axis) and the size of the field intensity spot with the desired -0.5-dB uniformity and edge illumination level (right axis) versus distance from the antenna aperture.
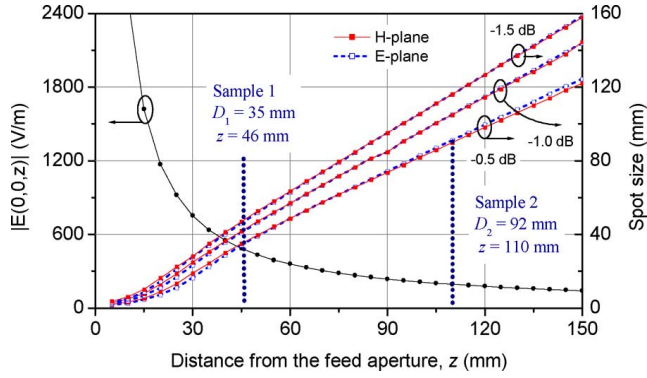
Fig. 8. Simulated E-field along the antenna physical axis and size of the field intensity spot for three exposure uniformity conditions versus distance from the antenna aperture. The exposure distances for samples 1 and 2 providing the desired -0.5-dB exposure uniformity are denoted by vertical dashed lines.
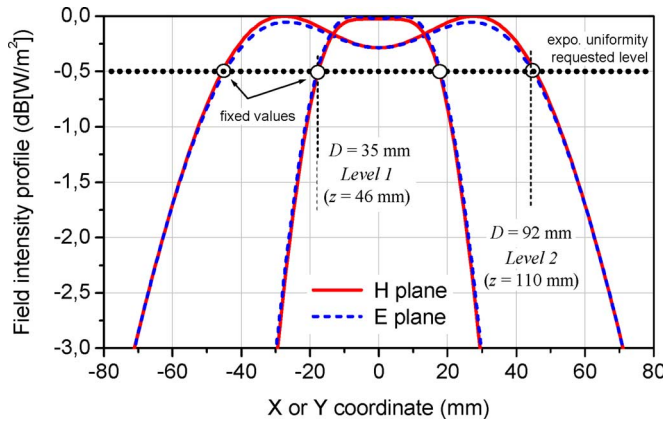

Fig. 9. Normalized field intensity distribution computed in xy-plane at certain distances from the antenna aperture at 60 GHz. SUT dimensions are denoted by vertical dashed lines.

TABLE I
SIMULATED EXPOSURE CHARACTERISTICS OF THE PROPOSED CRA AT 60 GHz

Sample 1 (D = 35 mm)		
-0.5 dB(W/m^2) exposure uniformity		
- optimal exposure distance, mm		46.0
- spot symmetry		0.98
- peak power density *, mW/cm^2		28.5
- exposure efficiency, %		55.8
-1.0 dB(W/m^2) exposure uniformity		
- optimal exposure distance, mm		40.0
- spot symmetry		0.98
- peak power density *, mW/cm^2		37.7
- exposure efficiency, %		63.0

Sample 2 (D = 92 mm)		
-0.5 dB(W/m^2) exposure uniformity		
- optimal exposure distance, mm		110.0
- spot symmetry		1.01
- peak power density *, mW/cm^2		5.0
- exposure efficiency, %		58.4
-1.0 dB(W/m^2) exposure uniformity		
- optimal exposure distance, mm		97.0
- spot symmetry		1.00
- peak power density *, mW/cm^2		6.4
- exposure efficiency, %		65.1

* - For the input power of 1W.

TABLE II
GEOMETRY AND DIMENSIONS OF THE REFERENCE FEEDS

	Ref. 1	Ref. 2	Ref. 3	Ref. 4
Reference feeds (all dimensions are in mm)				
Gain at 60GHz	8.0 dBi	16.2 dBi	9.0 dBi	21.5 dBi

The former is calculated based on the total input power of 1 W. The latter (i.e., spot dimensions) is determined based on the Poynting vector distributions in the xy-plane. The pairs of solid and dashed curves denote the spot size in the H- and E-planes, respectively. The additional curves are plotted for the exposure uniformity levels of -1.0 and -1.5 dB; they illustrate steepness of the slope at the spot edge (the closer the curves for different edge illumination levels, the steeper the slope, and thus, higher exposure efficiency can be achieved).

The optimal exposure distances for scenarios 1 and 2 for the exposure uniformity of -0.5 dB are denoted in Fig. 8 by vertical dashed lines. The corresponding field intensity distributions in the targets planes are shown in Fig. 9. As we can see, the symmetry is perfectly preserved for both exposure distances, whereas the field distribution slightly changes (i.e., $\sim$0.3-dB decay of the field intensity at the antenna physical axis is observed at level 2). Nevertheless, the desired -0.5-dB uniformity condition is fully satisfied at both levels.

Finally, the major exposure characteristics of the CRA are summarized in Table I for both samples and exposure uniformities of -0.5 and -1.0 dB. The optimal exposure distance, spot symmetry, and exposure level are extracted from Fig. 7. The spot symmetry is defined as a ratio between the field intensity spot dimensions in E- and H-planes. The power density at

the antenna axis is calculated as $P_D = P_{\text{rad}} G / (4\pi H^2)$, where $P_{\text{rad}} = 1$ W, G is the CRA boresight gain, i.e., 8.8 dBi at 60 GHz (Fig. 7), and H is the optimal exposure distance. The exposure efficiency is calculated as explained in Section II-C.

Benchmarking with the reference open-ended waveguide and horn feeds typically used for millimeter-wave exposure systems (see Tables II and III) reveals significant advantages of the reported CRA both in terms of the reduced exposure distance (the reduction constitutes a factor of 2–8, depending on the reference feed type) and enhanced exposure efficiency (factor of 2–1.5, respectively). The relative increase of the incident power density at the SUT surface constitutes a factor of 3–6, depending on the reference feed.

D. Visualization of the Near-Zone Field Intensity Distribution

To visualize the field intensity distribution at the sample surface, we use the infrared (IR) imaging technique presented in [28]. As demonstrated in [28] and [29], the highly localized superficial absorption in water at millimeter waves enables one to reconstruct the field intensity distribution on the surface of a water-based semi-solid phantom by recording the initial temperature rise rate and heating pattern on the phantom surface using a high-resolution IR camera.

TABLE III
SIMULATED EXPOSURE CHARACTERISTICS OF THE REFERENCE FEEDS

		Ref. 1	Ref. 2	Ref. 3	Ref. 4
Sample 1 (D = 35 mm)	**-0.5 dB(W/m²) exposure uniformity**				
	- exposure distance, mm	95	270	95	380
	- spot symmetry,	0.85	0.29	0.98	1.16
	- peak power dens.*, mW/cm²	5.6	4.6	7.0	8.0
	- exposure efficiency, %	27.8	27.6	30.0	37.4
	-1.0 dB(W/m²) exposure uniformity				
	- exposure distance, mm	68	210	66	265
	- spot symmetry	0.83	0.37	0.98	1.16
	- peak power dens.*, mW/cm²	10.9	7.5	14.5	16.4
	- exposure efficiency, %	36.8	34.5	40.3	48.5
Sample 2 (D = 92 mm)	**-0.5 dB(W/m²) exposure uniformity**				
	- exposure distance, mm	245	> 600	240	> 600
	- spot symmetry	0.85		0.99	
	- peak power dens.*, mW/cm²	0.8	n/a **	1.1	n/a **
	- exposure efficiency, %	27.5		30.1	
	-1.0 dB(W/m²) expo uniformity				
	- exposure distance, mm	170	435	167	> 600
	- spot symmetry	0.88	0.37	0.98	
	- peak power dens.*, mW/cm²	1.7	1.8	2.3	n/a **
	- exposure efficiency, %	37.2	40.1	40.4	

* - For the input power of 1W,　** - The exposure distance is larger
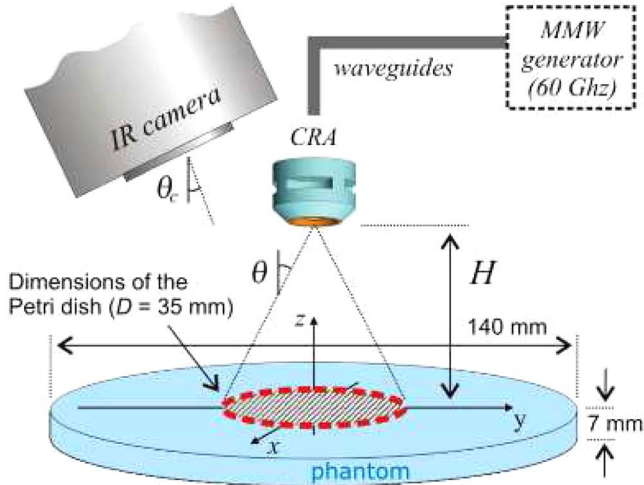than the height of a typical exposure chamber.

Fig. 10. Schematic drawing of the experimental setup used for visualization of the antenna near-field patterns (not to scale).

In the reported study, the thermal images are recorded using the IR camera FLIR SC5000 (FLIR Systems, Portland, OR, USA) operating in the 2.5–5.1-μm spectral range; its sensitivity and surface resolution are $0.025\,^{\circ}$C and $0.25\,\text{mm}^2$, respectively. The description of the experimental setup and methodology is presented in [28], and thus omitted here.

In the experiment, we use a 4%-agar phantom, as reported in [28]. Due to the high water concentration, its permittivity is close to that of free water ($\varepsilon = 11.9 - j19.5$ at 60 GHz and $20\,^{\circ}$C). The phantom is fabricated in a shape of a thin cylinder and illuminated from the top by the reported CRA (Fig. 10). The thermal image is recorder by the camera, which is slightly tilted to avoid the antenna shadow.
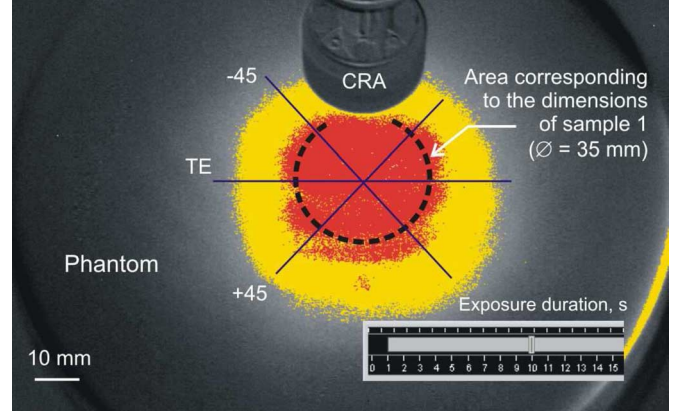

Fig. 11. Heating pattern recorder at the surface of the phantom illuminated by the CRA positioned at $z = 48.0$ mm. The spots with -1- and -3-dB uniformity levels are highlighted in red and yellow colors (in online version), respectively.
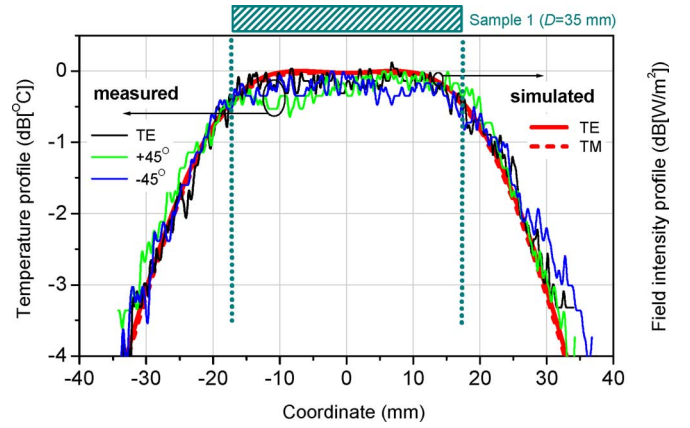

Fig. 12. Measured temperature profiles (left axis) and simulated field intensity distribution (right axis). The family of three curves for the thermal profiles depict the cut planes shown in Fig. 11. Simulated intensity profiles are the same as in Fig. 9, level 1.

It is worth mentioning that IR imaging of a Petri dish illuminated, as shown in Fig. 2(a), is more difficult because of the high absorption of the IR spectra by the polystyrene. Due to this, the phantom-based imaging approach is chosen.

To estimate the optimal exposure distance, a series of experiments is conducted by varying the distance between the antenna and sample plane with an increment of 1 mm. A representative thermal image taken for the exposure distance of $z = 48.0$ mm is shown in Fig. 11. This distance is considered as the optimal one because this is the minimum distance at which the -0.5-dB exposure uniformity condition is satisfied (Fig. 12). The minor asymmetry of the thermal spot and discrepancies between the measured temperature profiles and simulated field intensity distribution is due to several factors: minor roughness of the phantom surface, excitation of the so-called Zenneck surface wave, which can be excited in the E-plane (TM polarization) on the surface of a lossy dielectric [30], and the slight difference between the Fresnel reflection coefficients for the TE and TM waves incident on the air–dielectric interface under angles $\theta > 0°$. For the plane wave incident on the air/phantom interface at $\theta = 30°$ (i.e., SUT edge direction) this difference
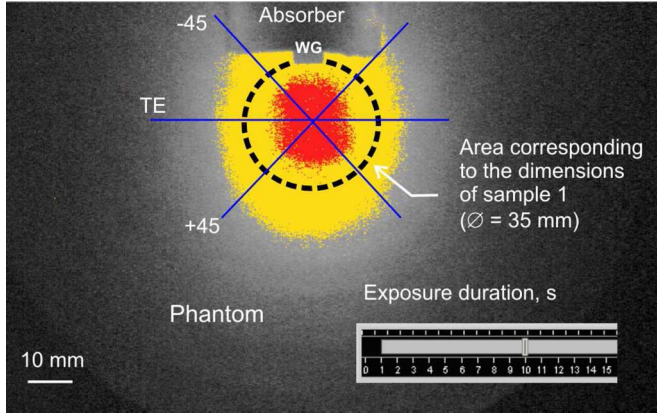
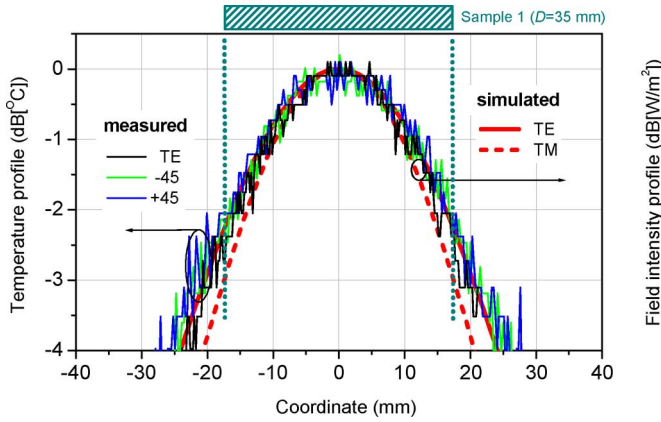Fig. 13. Same as in Fig. 10 for the rectangular waveguide (WR-15) positioned at $z = 40.0$ mm.

Fig. 14. Measured temperature profiles (left axis) and simulated field intensity (right axis) in the xy-plane at $z = 40.0$ mm for the waveguide feed.

equals ~10%, whereas for $\theta = 45°$, it exceeds 24%. A quantitative estimate of the surface wave impact requires deeper investigation because it strongly depends on the excitation conditions and surface roughness.

Unfortunately, the low signal-to-noise ratio prevents reliable visualization of the field distributions at larger distances ($z \sim 110$ mm) corresponding to scenario 2. Nevertheless, the very good agreement between the simulated and experimental data observed for both radiation and exposure characteristics for scenario 1 confirms credibility of the specifications given in Table I for both scenarios.

Finally, Fig. 13 shows the temperate profile produced by a standard rectangular waveguide (WR-15) irradiating the same phantom from the distance of $z = 40.0$ mm. This distance is selected in order to provide the same 55% exposure efficiency achieved for the CRA with -0.5-dB exposure uniformity. In the experiment, the waveguide flange is covered by an absorber to diminish parasitic back reflections from the waveguide flange. A very good agreement between the temperature and field intensity profiles has been achieved, which confirms the accuracy of the IR imaging approach (Fig. 14).

As we can see in Fig. 14, the edge illumination obtained using the waveguide feed is about -3.0 and -2.2 dB for the E(TM)

Fig. 15. Simulated E-field magnitude along the antenna physical axis and dimensions of the field intensity spot with a desired uniformity level versus distance from the antenna aperture. (a) Ref. 1: rectangular horn. (b) Ref. 2: pyramidal horn. (c) Ref. 3: circular waveguide. (d) Ref. 4: conical horn. The optimal exposure distances for both samples are denoted by vertical dashed lines (when applicable). Total antenna input power is 1 W.

and H(TE) waves, respectively, which is considered insufficient. Note that one can achieve the desired -0.5-dB exposure

uniformity using the waveguide feed by increasing the exposure distance up to 95 mm; however, the exposure efficiency will decrease to 27.8% (see Table III).

IV. CONCLUSION

The possibility for improving the exposure efficiency and uniformity of a radiation-type millimeter-wave exposure setup has been demonstrated by introducing a novel CRA, whose characteristics have been optimized to achieve the best possible exposure efficiency under the -0.5-dB exposure uniformity requirement.

The antenna prototype has been fabricated in metallized foam. Its far-field characteristics have been measured and found to be in a good agreement with simulations. The field intensity distributions on the surface of the sample have been visualized using the IR imaging approach.

The reference data for standard waveguide feeds, commonly used for *in vitro* bioelectromagnetic studies at millimeter waves, have also been presented. Advantages of the proposed CRA are demonstrated in terms of: 1) enhanced exposure efficiency; 2) reduced exposure distance; and 3) increased incident power density. The superior performance characteristics of the reported CRA make it a favorable choice for short-range millimeter-wave exposure systems.

APPENDIX

This section presents the exposure characteristics of standard waveguide feeds used in earlier *in vitro* experiments at millimeter waves, namely, open-ended rectangular and circular waveguides [8], [28], pyramidal horn [3]–[10], and conical horn [2], [5], [7]. Where appropriate, the dimensions of the reference antennas are scaled to fit the 60-GHz operational frequency (Table II).
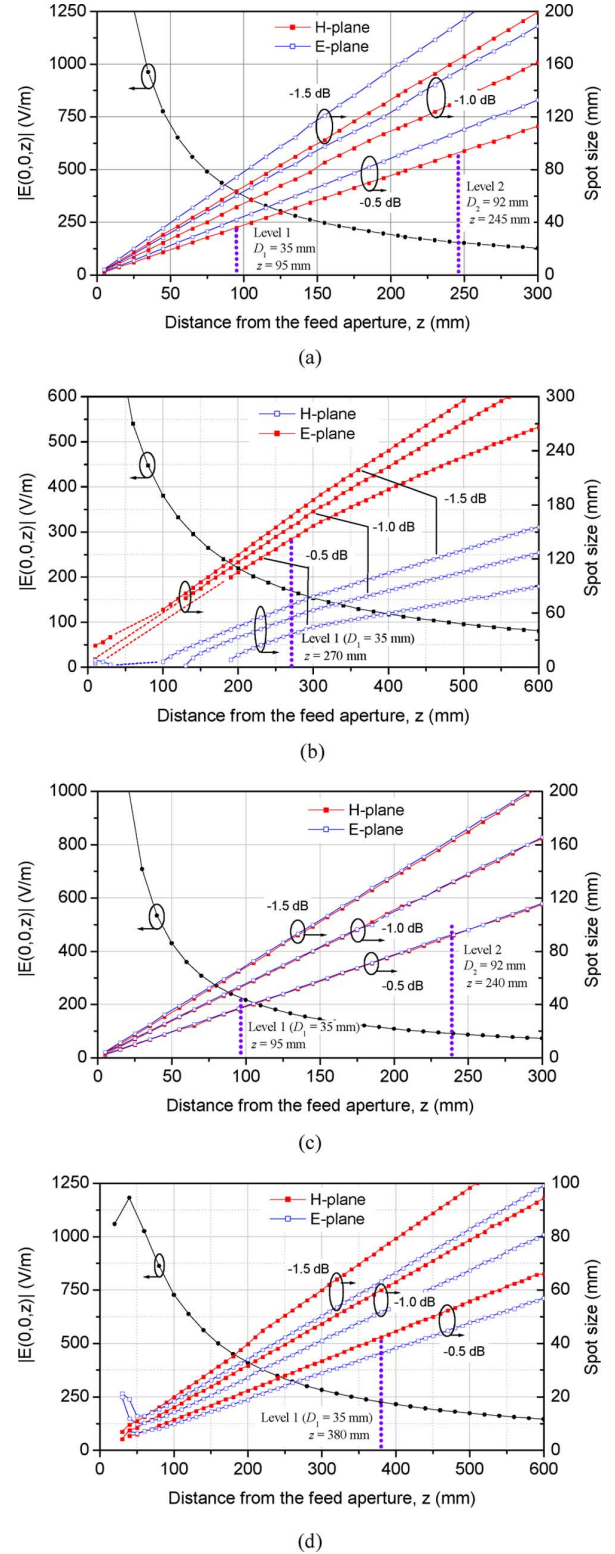
Fig. 15 presents the *E*-field magnitude along the antenna physical axis (left axis) and dimensions of the field intensity spot with a desired uniformity and edge illumination level (right axis) versus distance from the antenna aperture (same as in Fig. 8). The spot size is determined based on the Poynting vector distribution in xy-plane. The two curves denote the spot size in both principal planes. The optimal exposure distances for both SUTs are denoted by vertical dashed lines. Note that, in some cases, the exposure distance is prohibitively large (i.e., reference antennas 2 and 4 in scenario 2).

The major exposure characteristics, relevant to the reported study, are summarized in Table III. As we can see, the most commonly used rectangular horn suffers from the pattern asymmetry, which spoils its exposure efficiency. A better symmetry and efficiency is achieved using circular feeds. In particular, the best performance for scenario 1 is achieved for the conical horn, but this feed requires large exposure distance; this raises certain difficulties in positioning of the sample and increases total size of the experimental setup, which may become prohibitively large as it happens for scenario 2. This prevents its utilization in short-range exposure systems.

REFERENCES

[1] M. Zhadobov, N. Chahat, R. Sauleau, C. Le Quément, and Y. Le Dréan, "Millimeter-wave interactions with the human body: State of knowledge and recent advances," *Int. J. Microw. Wireless Technol.*, vol. 3, pp. 237–247, 2011.

[2] H. A. Kues, S. A. D'Anna, R. Osiander, W. R. Green, and J. C. Monahan, "Absence of ocular effects after either single or repeated exposure to 10 mW/cm² from a 60 GHz CW source," *Bioelectromagnetics*, vol. 20, no. 8, pp. 463–473, 1999.

[3] J. X. Zhao, "Numerical dosimetry for cells under millimetre-wave irradiation using Petri dish exposure setups," *Phys. Med. Biol.*, vol. 50, pp. 3405–3421, 2005.

[4] J. Zhao and Z. Wei, "Numerical modeling and dosimetry of the 35 mm Petri dish under 46 GHz millimeter wave exposure," *Bioelectromagnetics*, vol. 26, no. 6, pp. 481–488, 2005.

[5] M. Zhadobov, R. Sauleau, V. Vié, M. Himdi, L. Le Coq, and D. Thouroude, "Interactions between 60-GHz millimeter waves and artificial biological membranes: Dependence on radiation parameters," *IEEE Trans. Microw. Theory Techn.*, vol. 54, no. 6, pp. 2534–2542, Jun. 2006.

[6] M. Zhadobov, Ch. Nicolas Nicolaz, R. Sauleau, F. Desmots, D. Thouroude, D. Michel, and Y. Le Dréan, "Evaluation of the potential biological effects of millimeter waves at 60.42 GHz upon human cells," *IEEE Trans. Antennas Propag.*, vol. 57, no. 10, pp. 2949–2956, Oct. 2009.

[7] S. Kurogi, H. Saito, T. Taguchi, Y. Suzuki, and M. Taki, "Development and dosimetry of a free-space type *in vitro* exposure apparatus for millimeter-waves," in *Proc. Int. Electromagn. Compat. Symp.*, Kyoto, Japan, 2009, pp. 313–316.

[8] P. Siegel and V. Pikov, "Impact of low intensity millimeter waves on cell functions," *Electron. Lett.*, vol. 46, no. 26, pp. 70–72, 2010.

[9] C. Le Quément, C. N. Nicolaz, M. Zhadobov, F. Desmots, R. Sauleau, M. Aubry, D. Michel, and Y. Le Dréan, "Whole-genome expression analysis in primary human keratinocyte cell cultures exposed to 60 GHz radiation," *Bioelectromagnetics*, vol. 33, no. 2, pp. 147–158, 2012.

[10] M. Zhadobov, R. Sauleau, R. Augustine, C. Le Quément, Y. Le Dréan, and D. Thouroude, "Near-field dosimetry for *in-vitro* exposure of human cells at 60 GHz," *Bioelectromagnetics*, vol. 33, no. 1, pp. 55–64, 2012.

[11] A. Paffi, F. Apollonio, G. A. Lovisolo, C. Marino, R. Pinto, M. Repacholi, and M. Liberti, "Considerations for developing an RF exposure system: A review for *in-vitro* biological experiments," *IEEE Trans. Microw. Theory Techn.*, vol. 58, no. 10, pp. 2702–2714, Oct. 2010.

[12] G. A. Lovisolo, F. Apollonio, L. Ardoino, M. Liberti, V. Lopresto, C. Marino, A. Paffi, and R. Pinto, "Specifications of *in vitro* exposure setups in the RF range," ITIS-ETHZ, Zurich, Switzerland, 2005. [Online]. Available: http://www1.itis.ethz.ch/mv/downloads/DAY1/1C-Lovisolo-s.pdf

[13] M. A. Stuchly, S. S. Stuchly, and G. Kantor, "Diathermy applicators with circular aperture and corrugated flange," *IEEE Trans. Microw. Theory Techn.*, vol. MTT-28, no. 3, pp. 267–271, Mar. 1980.

[14] A. A. Kishk, "Simple primary focus feeds for deep reflectors," *Proc. Inst. Elect. Eng.*, vol. 136, no. 2, pp. 169–171, 1989.

[15] L. Shafai and A. A. Kishk, , A. D. Olver, Ed., "Prime focus waveguide feeds," in *Microwave Horns and Feeds*. Piscatway, NJ, USA: IEEE Press, 1994.

[16] Q. Zhang, C.-W. Yuan, and L. Liu, "A coaxial corrugated dual-band horn feed," *IEEE Antennas Wireless Propag. Lett.*, vol. 8, pp. 1357–1359, Aug. 2009.

[17] R. Lehmensiek and D. I. L. de Villiers, "Wide flare angle axially corrugated conical horn design for a classical offset dual-reflector antenna," in *Proc. Eur. Antennas Propag. Conf.*, Prague, Czech Republic, 2012.

[18] Z. Allahgholi Pour and L. Shafai, "A ring choke excited compact dual-mode circular waveguide feed for offset reflector antennas," *IEEE Trans. Antennas Propag.*, vol. 60, no. 6, pp. 3011–3015, Jun. 2012.

[19] J. Galvan and D. Colantonio, "Low back radiation compact antenna for data downlink in LEO satellites," in *Proc. Int. Microw. Optoelectron. Conf.*, 2009, pp. 816–820.

[20] Y. B. Karandikar and P.-S. Kildal, "$X-Ka$ dual band prime focus feed for satellite earth terminals," in *Proc. Eur. Antennas Propag. Conf.*, Berlin, Germany, Mar. 2009, pp. 3085–3089.

[21] J. Lizarraga, G. Crespo, and C. del Rio, "Discrete lenses for multibeam applications," in *Proc. Eur. Antennas Propag. Conf.*, Rome, Italy, Apr. 2011, pp. 3513–3517.

[22] F. Sciré-Scappuzzo and S. N. Makarov, "A low-multipath wideband GPS antenna with cutoff or non-cutoff corrugated ground plane," *IEEE Trans. Antennas Propag.*, vol. 57, no. 1, pp. 33–46, Jan. 2009.

[23] S. Steshenko, A. A. Kirilenko, A. V. Boriskin, M. Zhadobov, and R. Sauleau, "Advanced modeling of choke ring antennas for mm-wave applications," in *Proc. Eur. Antennas Propag. Conf.*, Prague, Czech Republic, 2012, pp. 650–654.

[24] S. Steshenko, A. A. Kirilenko, A. V. Boriskin, M. Zhadobov, and R. Sauleau, "H-plane radiation patterns of rectangular waveguide aperture with a corrugated flange," in *Proc. Int. Math. Methods Electromagn. Theory Conf.*, Kharkov, Ukraine, 2012, pp. 476–479.

[25] A. Rolland, N. T. Nguyen, R. Sauleau, C. Person, and L. Le Coq, "Smooth-walled light-weight Ka-band shaped horn antennas in metallized foam," *IEEE Trans. Antennas Propag.*, vol. 60, no. 3, pp. 1245–1251, Mar. 2011.

[26] A. Rolland, A. V. Boriskin, C. Person, L. Le Coq, and R. Sauleau, "Lens-corrected axis-symmetrical shaped horn antenna in metallized foam with improved bandwidth," *IEEE Antennas Wireless Propag. Lett.*, vol. 11, no. 1, pp. 57–60, 2012.

[27] FEKO Electromagnetic Software. FEKO, Stellenbosch, South Africa. [Online]. Available: http://www.feko.info

[28] N. Chahat, M. Zhadobov, R. Sauleau, and S. I. Alekseev, "New method for determining dielectric properties of skin and phantoms at millimeter waves based on heating kinetics," *IEEE Trans. Microw. Theory Techn.*, vol. 60, no. 3, pp. 827–832, Mar. 2012.

[29] N. Chahat, M. Zhadobov, and R. Sauleau, "Broadband tissue-equivalent phantom for BAN applications at millimeter waves," *IEEE Trans. Microw. Theory Techn.*, vol. 60, no. 7, pp. 2259–2266, Jul. 2012.

[30] H. R. Barlow and A. L. Cullen, "Surface waves," *Proc. Inst. Elect. Eng.*, vol. 100, no. 63, pp. 329–341, Nov. 1953.

Artem V. Boriskin (S'99–M'04–SM'12) was born in Kharkov, Ukraine, in 1977. He received the M.S. degree (*cum laude*) in radiophysics and electronics from Kharkov National University, Kharkov, Ukraine, in 1999, and the Ph.D. degree in radiophysics from IRE NASU, Kharkov, Ukraine, in 2004.

From 1999 to 2009, he was with the Department of Computational Electromagnetics, IRE NASU, where his final position was as a Senior Research Scientist. During that time, he spent short appointments with Bilkent University, Bilkent, Turkey, IT-Warsaw, Warsaw, Poland, and the University of Nottingham, Nottingham, U.K. He also visited the Institut d'Electronique et de Télécommunications de Rennes (IETR), Université de Rennes 1, Rennes, France, numerous times. Since August 2009, he has held a post-doctoral position with IETR with the Antennas and Microwave Devices Group. He has authored or coauthored over 90 scientific publications. His research interests are computational electromagnetics and antenna design with an emphasis on millimeter-wave antennas and dielectric-based focusing devices.

Dr. Boriskin was a head of the Young Scientist Council, Institute of Radiophysics and Electronics of the National Academy of Sciences of Ukraine (IRE NASU), from 2004 to early 2008. From 2007 to 2009, he was a founder and faculty adviser of the local student chapter of the Optical Society of America (OSA) at IRE NASU, which was recognized as the best midsize OSA Chapter in 2008. In 2009, he was a mentor for the IEEE IRE-Kharkov Student Branch. From 2002 to 2012, he was a member of the Organizing Committee and Technical Program Committee (TPC) and secretary and publication chair of multiple national and international conferences. Since 2010, he has been a scientific secretary of the ESF Research Networking Program NEWFOCUS, which is devoted to integrated dielectric focusing systems at millimeter and submillimeter waves. He was the recipient of several awards including IEEE Microwave Theory and Techniques Society (IEEE MTT-S) Graduate Fellowship Award in 2000, the First Microwave Prize of the European Microwave Association (EuMA) at MSMW-2004, and the Second Award of the Samsung Corporation at the National Research Project Contest in 2005. He was the recipient of the highest National Young Scientist Award and a medal "For the contribution to development of Ukraine" from the Cabinet of Ministers of Ukraine in 2009.

Maxim Zhadobov (S'05–M'07) received the M.S. degree in radiophysics from N. Novgorod State University, N. Novgorod, Russia, in 2003, and the Ph.D. degree in bioelectromagnetics from the Institut d'Electronique et de Télécommunications de Rennes (IETR), Université de Rennes 1, Rennes, France, in 2006.

In 2008, he completed post-doctoral training with the Center for Biomedical Physics, Temple University, Philadelphia, PA, USA. He then rejoined IETR, as an Associate Researcher with the Centre National de la Recherche Scientifique (CNRS). His main scientific interests and research activities are focused on interactions of microwaves, millimeter waves, and pulsed radiations with the human body, including electromagnetic modeling and characterization, biocompatibility of emerging wireless communication systems, biomedical applications of nonionizing radiations, antennas and propagation for body-centric networks, and experimental and numerical electromagnetic dosimetry.

Dr. Zhadobov was the recipient of the 2005 Best Poster Presentation Award from the International School of Bioelectromagnetics, the 2006 Best Scientific Paper Award from the Bioelectromegnetics Society, and the 2010 Brittany's Young Scientist Award.

Sergiy Steshenko (M'03) received the M.S. degree in applied mathematics from Kharkiv National University, Kharkiv, Ukraine, in 1996, and the Ph.D. degree in radiophysics from the Institute of Radiophysics and Electronics of the National Academy of Sciences of Ukraine (IRE NASU), Kharkiv, Ukraine, in 2006.

From 2001 to 2005, he was with the Department of Mathematics, Kharkiv National University, as a Junior Scientist. He is currently a Senior Research Scientist with the Department of Computational Electromagnetics, IRE NASU. From 2007 to 2008 and 2010, he was a Postdoctoral Fellow with the Department of Information Engineering, University of Siena, Siena, Italy. He recently had a few short-term visits with the Institut d'Electronique et de Télécommunications de Rennes (IETR), Université de Rennes 1, Rennes, France. His current research interests are numerical methods for the analysis and design of waveguides and antennas and eigenvalue problems.

Yves Le Dréan was born in 1964. He received the Ph.D. degree and Habilitation à Diriger des Recherches degree in biology from the Université de Rennes 1, Rennes, France, in 1993 and 2007, respectively.

In 1994, he joined the Hospital for Sick Children, Toronto, ON, Canada, as a Post-Doctoral Fellow. Since 1997, he has been an Associate Professor with the Université de Rennes 1, where he teaches molecular biology and biochemistry. His main subject of interest is the control of genetic expression. His current research activities are related to the investigations of cell responses to environmental stress. Since 2004, he has been also actively involved in the field of biological effects of electromagnetic waves. He has authored or coauthored two book chapters, 35 journal publications, and 55 communications in national and international conferences.

Laurent Le Coq received both the Electronic Engineering and Radiocommunications degree and the French DEA degree (M.Sc.) in electronics and Ph.D. degree from the National Institute of Applied Science (INSA), Rennes, France, in 1995 and 1999, respectively.

In 1999, he joined the Institut d'Electronique et de Télécommunications de Rennes (IETR), Université de Rennes 1, Rennes, France, as a Research Laboratory Engineer, where he is responsible for measurement technical facilities up to 110 GHz. He has authored or coauthored 30 journal papers. His activities in antenna measure-

ments and development of related procedures involved him in more than 20 research contracts of national or European interest over the last five years. He is in charge of measurements system use, equipment evolution and post-processing development. His area of interest concerns alignment using electrical measurements, phase center determination, system error compensations, and measurement system capabilities optimization.

Christian Person (M'11–SM'12) received the Ph.D. degree in electronics from the University of Brest, Brest, France, in 1994.

Since 1991, he has been an Assistant Professor with the Microwave Department, École Nationale Supérieure des Télécommunications de Bretagne, Brest, France. In 2003, he became a Full Professor with the Mines-Telecom Institute/Telecom Bretagne, Brest, France, where he currently conducts research with the Lab-STICC Laboratory (Information and Communication Science and Technology Laboratory), UMR CNRS 6285. He also contributes to the foundation of the WHIST Laboratory, a joined laboratory between the Telecom Institute and Orange Laboratories that deal with electromagnetic modeling and evaluation of interaction between microwaves and the human body. He is involved in the development of new technologies for microwave and millimeter-wave applications and systems. His activities are especially focused on the design of passive functions (filters and couplers) and antennas, providing original solutions in terms of synthesis techniques, analysis, and optimization procedures, as well as technological implementation (foam, plastic, low-temperature co-fired ceramic (LTCC), etc.). He is also concerned with RF integrated front-ends on silicon. He is currently involved in different French and European research programs dealing with system-on-chip (SoC)/system-in-package (SiP) antennas and reconfigurable structures for smart systems in the (0.4–140 GHz and above) frequency range. Since 2002, he has been an Expert on the mobile phone SAR certification process with the Cofrac Institute. He is involved in numerous research investigations dealing with microwave and human body interactions for both modeling and measuring activities. These contributions also address emerging applications such as body area networks (BANs) and wireless sensors networks.

Ronan Sauleau (M'04–SM'06) graduated in electrical engineering and radio communications from the Institut National des Sciences Appliquées, Rennes, France, in 1995. He received the Agrégation degree from the École Normale Supérieure de Cachan, Cachan, France, in 1996, and the Doctoral degree in signal processing and telecommunications and the "Habilitation à Diriger des Recherches" degree from the Université de Rennes 1, Rennes, France, in 1999 and 2005, respectively.

From September 2000 to November 2005, and from December 2005 to October 2009, he was an Assistant Professor and Associate Professor, respectively, with the Université de Rennes 1. In November 2009, he became a Full Professor with the Université de Rennes 1. His current research fields are numerical modeling [mainly finite difference time domain (FDTD)], millimeter-wave printed and reconfigurable [microelectromechanical systems (MEMS)] antennas, substrate integrated waveguide antennas, lens-based focusing devices, periodic and nonperiodic structures (electromagnetic-bandgap materials, metamaterials, reflectarrays, and transmitarrays), and biological effects of millimeter waves. He has been involved in over 30 research projects at the national and European levels. He has co-supervised 14 post-doctoral fellows, 18 doctoral students, and 40 master students. He has authored or coauthored over 135 journal papers and 290 publications in international conferences and workshops. He holds eight patents. In 2010 and 2011, he shared the responsibility of the research activities on antennas at the Institut d'Electronique et de Télécommunications de Rennes (IETR), Université de Rennes 1. He is currently co-responsible for the Antenna and Microwave Devices Department, IETR, where he is also th Deputy Director.

Prof. Sauleau was a guest editor for the IEEE TRANSACTIONS ON ANTENNAS AND PROPAGATION "Special Issue on Antennas and Propagation at Millimeter and Submillimeter Waves" (2013). In 2007, he was elevated to a Junior Member of the Institut Universitaire de France. He was the recipient of the 2004 ISAP Conference Young Researcher Scientist Fellowship (Japan) and the first Young Researcher Prize, Brittany, France, in 2001 for his research on gain-enhanced Fabry–Perot antennas. He was the recipient of the Bronze Medal of CNRS in 2008. He was the corecipient of several international conference awards (International School of BioEM 2005, BEMS'2006, MRRS'2008, E-MRS'2011, BEMS'2011, IMS'2012,and Antem'2012).